

# NAS-PRNet: Neural Architecture Search generated Phase Retrieval Net for Off-axis Quantitative Phase Imaging

Xin Shu<sup>1</sup>, Mengxuan Niu<sup>1</sup>, Yi Zhang<sup>1</sup>, and Renjie Zhou<sup>1,\*</sup>

<sup>1</sup>Department of Biomedical Engineering, the Chinese University of Hong Kong, Shatin, New Territories, Hong Kong, China

\*Corresponding author: [rjzhou@cuhk.edu.hk](mailto:rjzhou@cuhk.edu.hk)

**Abstract:** Single neural networks have achieved simultaneous phase retrieval with aberration compensation and phase unwrapping in off-axis Quantitative Phase Imaging (QPI). However, when designing the phase retrieval neural network architecture, the trade-off between computation latency and accuracy has been largely neglected. Here, we propose Neural Architecture Search (NAS) generated Phase Retrieval Net (NAS-PRNet), which is an encoder-decoder style neural network, automatically found from a large neural network architecture search space. The NAS scheme in NAS-PRNet is modified from SparseMask, in which the learning of skip connections between the encoder and the decoder is formulated as a differentiable NAS problem, and the gradient decent is applied to efficiently search the optimal skip connections. Using MobileNet-v2 as the encoder and a synthesized loss that incorporates phase reconstruction and network sparsity losses, NAS-PRNet has realized fast and accurate phase retrieval of biological cells. When tested on a cell dataset, NAS-PRNet has achieved a Peak Signal-to-Noise Ratio (PSNR) of 36.1 dB, outperforming the widely used U-Net and original SparseMask-generated neural network. Notably, the computation latency of NAS-PRNet is only 31 ms which is 12 times less than U-Net. Moreover, the connectivity scheme in NAS-PRNet, identified from one off-axis QPI system, can be well fitted to another with different fringe patterns.

---

## 1. INTRODUCTION

Quantitative Phase Imaging (QPI) has been widely applied to biomedical imaging [1, 2] and material metrology [3, 4]. In off-axis interferometry-based QPI [5] (off-axis QPI), the Optical Path Difference (OPD) or phase distribution of an object is encoded in a fringe pattern or interferogram by interfering the object field with a tilted reference field. To reconstruct the phase map from a recorded interferogram, the conventional approach contains three key steps: (i) retrieving the wrapped phase (valued between 0 to  $2\pi$ ) from the complex object field (e.g., using the Fourier transform method [6]); (ii) unwrapping the phase (e.g., using the Goldstein algorithm [7]); and (iii) calibrating the phase or compensating the phase aberration by using an additional interferogram captured in a sample-free region [8]. Among the three steps, phase unwrapping is the most time-consuming; moreover, one may fail to obtain the calibration interferogram when imaging a dense sample. To expedite phase retrieval in off-axis QPI, parallel computation using sophisticated Parallel Graphics Processing Units (GPUs) or Field Programmable Gate Arrays (FPGAs) has been applied to accelerate phase unwrapping [9, 10], while the calibration interferogram is still required. In recent years, neural networks have become attractive alternatives for achieving phase retrieval with aberration compensation with/without phase unwrapping in off-axis QPI, such as the widely used U-Net models [11, 12] and the Y-Net [13]. Despite realizing significant simplification of the imaging system and reduced cost, furthering applying those methods for real-time phase imaging in off-axis QPI is potentially limited by the relatively large computation latency and phase retrieval accuracy. It is known that the network inference accuracy and efficiency heavily depend on its architecture. Therefore, a strategy to identify an optimal network architecture is needed to minimize the computation latency, while keeping the phase retrieval accuracy high.

Neural architecture search (NAS) [14] is a technique to automatically find an optimal network architecture from a large architecture search space. NAS generated networks have outperformed manually designed networks in many tasks, including classification [15-17] and end-to-end dense image prediction (e.g., semantic segmentation and stereo depth reconstruction) [18-21]. SparseMask [22] is an end-to-end dense image prediction NAS scheme. SparseMask has a search space that covers different skip connection strategies from the encoder to the decoder, which enables searching for optimal ways to fuse low-level features rich in spatial details and high-level features containing semantic information. In SparseMask, differentiable NAS search strategy [23] is used to relax the architecture search space from discrete to continuous, which can enable an efficient optimization of skip connections based on gradient decent. Taking both dense image prediction accuracy and connectivity sparsity into account, SparseMask attains comparable results while runs more than three times faster compared with the widely-used Pyramid Scene Parsing Network (PSPNet) [24] on semantic segmentation PASCAL VOC 2012 test dataset [25].

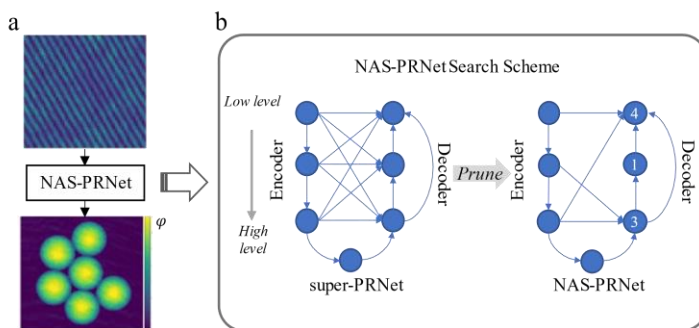


Fig. 1. Phase Retrieval Net (NAS-PRNet). (a) NAS-PRNet retrieves a phase map from an interferogram. (b) Search scheme for NAS-PRNet. Super-PRNet is the super-network covering the whole search space, and NAS-PRNet is the searched sparsely connected neural network. Blue circles in the schematics represent stages of the encoder and decoder, the lines with arrow represent connections from the head stage to the tail stage, the numbers in the decoder circles represent the number of input features.

For achieving accurate phase retrieval with high efficiency, we propose NAS generated Phase Retrieval Net (NAS-PRNet), as illustrated in Fig. 1. Before generating NAS-PRNet, an intermediate super-network for phase retrieval (denoted as super-PRNet in Fig. 1(b)), containing all the encoder and the decode connections, is firstly built up. After training the super-PRNet, the encoder and decoder connections are pruned according to the connection weights in super-PRNet to obtain the architecture of NAS-PRNet. Then, NAS-PRNet is trained and tested for phase retrieval. Both super-PRNet and NAS-PRNet are trained and tested with the same biological cell dataset. The search scheme for NAS-PRNet is modified from SparseMask but differs in two aspects: (1) encoder features are allowed to propagate into all stages of the decoder to enlarge the search space, while encoder features in SparseMask are only allowed to propagate into their corresponding lower-level decoder stages; (2) a global sparsity restrict is adopted to make the total number of connections as small as possible, while SparseMask uses a sparsity restrict for each decoder stage on a fixed quantity of connections. Moreover, the network structure of super-PRNet or NAS-PRNet, including output layer (i.e., adopting a regression head), feature fusing style, kernel size in convolution, feature depth strategy, etc., is customized for the phase retrieval problem.

## 2. METHODS AND PRINCIPLES

### A. Construction of Super-PRNet

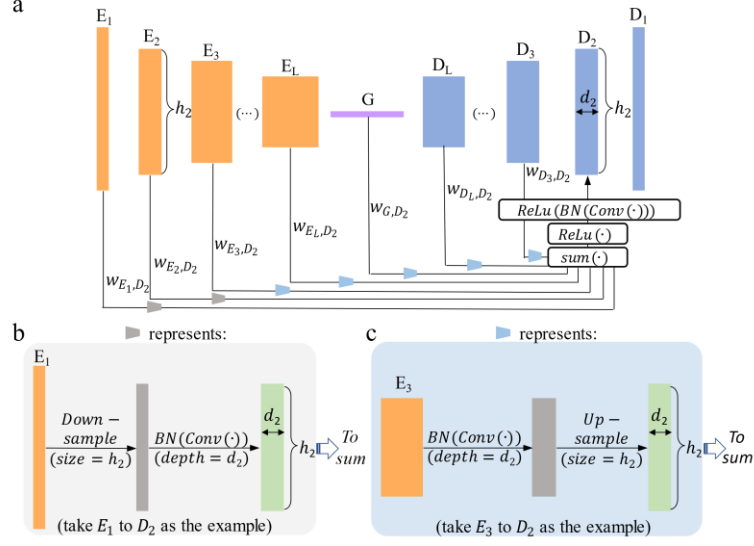


Fig. 2. Feature concatenation in super-PRNet. (a) Formation of  $D_2$ .  $E_i$ :  $i$ th encoder feature;  $D_j$ :  $j$ th decoder feature. (b) Processing of input features with spatial sizes larger than  $h_2$ . (c) Processing of input features with spatial sizes smaller than  $h_2$ .

The structure of super-PRNet is illustrated in Fig. 2. For expediting inference speed, MobileNet-v2 [26] is implemented as the encoder to extract multi-level features from an input interferogram. As shown Fig. 2(a), the encoder features at multiple levels are denoted as  $E_l$ , where  $l$  is the stage index ranging from 1 to  $L = 8$  (i.e., 8 encoder features are input to the decoder). In addition, a ground encoder feature,  $G$ , is obtained by applying an average pool with a target size of  $3 \times 3$ , and then input to the decoder. The decoder integrates all possible connections between encoder and decoder stages, as well as different stages inside the decoder. Being symmetric with the encoder, the number of stages in the decoder is also  $L$ .  $D_l$  denotes the  $l$ th decoder stage feature, and it has the same feature spatial size of  $h_l$  as  $E_l$ . The feature depth of  $D_l$  is set as  $\min(256, 8l)$ . For the  $l$ th encoder stage, its input features are  $\{E_i | 1 \leq i \leq L\}$ ,  $G$ , and  $\{D_j | l < j \leq L\}$ . As illustrated in Fig. 2(b) and (c), to efficiently fuse arbitrary input features differing in size and depth, a bilinear down-sampling with a target spatial size of  $h_l$  is first applied before a convolution with a target feature depth of  $d_l$  for features  $m \in M_l^+ = \{E_i | 1 \leq i < l\}$  whose spatial size is larger than  $h_l$ ; on the contrary, a convolution with a target feature depth of  $d_l$  is first applied before a bilinear up-sampling with a target spatial size of  $h_l$  for features  $m \in M_l^- = \{E_i | l \leq i \leq L\} \cup G \cup \{D_j | l < j \leq L\}$  whose spatial size is smaller than  $h_l$ . Then, the input features of the same depth and size are fused as a fused feature,  $T_l$ , by a weighted sum that weights the connections from input stages to the target stage, following:

$$T_l = \sum_{m \in M_l^+} w_{m,l} \text{bn}(\text{conv}(f_{\downarrow}(m))) + \sum_{m \in M_l^-} w_{m,l} \text{bn}(f_{\uparrow}(\text{conv}(m))), \quad (1)$$

where  $f_{\downarrow}()$  and  $f_{\uparrow}()$  denote the bilinear down-sampling and bilinear up-sampling, respectively;  $\text{conv}()$  is the 2D convolution with  $3 \times 3$  kernel size;  $\text{bn}()$  represents batch normalization; and  $w_{m,l}$  is the weight of the connection from input feature  $m$  to decoder  $D_l$  ( $w_{m,l} = 0$  indicates the connection does not exist;  $w_{m,l} = 1$  indicates the connection exist). Similar to SparseMask,  $\text{bn}()$  ensures the output value of  $\text{conv}(f_{\downarrow}())$  or  $f_{\uparrow}(\text{conv}())$  not affecting the connection importance represented by the summation weight ( $w_{m,l}$ ). Finally, decoder feature  $D_l$  is obtained as:

$$D_l = \text{ReLU6}\left(\text{bn}\left(\text{conv}\left(\text{ReLU6}(T_l)\right)\right)\right), \quad (2)$$

where  $\text{ReLu6}()$  is the nonlinear activation function [27]. To output a phase map with continuous phase values and same pixel size as the input interferogram in a single-channel, a regression head is added to the end feature  $D_1$  of the decoder. The regression head is comprised of three consecutive functions: (i) 2D convolution to compress the feature depth of  $D_1$  from 8 to 1; (ii) interpolation to make the feature spatial size of  $D_1$ , i.e.,  $h_1$ , identical to the input interferogram (originally  $h_1$  is only half the size of the interferogram); and (iii) ReLu6 nonlinear activation and dividing the obtained value by 6 to make the output have pixel value ranging from 0 to 1 for training.

## B. Training of Super-PRNet

The search for the optimal encoder and decoder connections for NAS-PRNet is formulated as a problem of finding the optimal binary subset of the weight set  $W = \{w_{m,l} | m \in M_l^+ \cup M_l^-, 1 \leq l \leq L\}$  by training the super-PRNet. Considering the tradeoff between efficiency and accuracy, the optimization objectives include (i) making the connectivity as sparse as possible to reduce the computation latency of this network; and (ii) decreasing the phase retrieval loss as much as possible. As it is computationally inefficient to search  $W$  on a discrete search space, we relax all weights  $w \in W$  to be continuous, ranging from 0 to 1, to allow for gradient descent to be used to conduct the architecture search. The synthesized loss function  $Loss_*$  used in the training process is formulated as:

$$Loss_* = Loss_t + \alpha Loss_b + \beta Loss_s, \quad (3)$$

where  $Loss_t$  is the phase reconstruction loss which is calculated as the Mixed Gradient Error (MixGE) between the ground truth and the network output as defined in [28];  $Loss_b$  and  $Loss_s$  are the weight binary loss and the network sparsity loss, respectively; and  $\alpha$  and  $\beta$  are the ratio for  $Loss_b$  and  $Loss_s$ .  $Loss_b$  and  $Loss_s$  are obtained as:

$$Loss_b = \frac{1}{len(W)} \sum_{w \in W} (-w \log(w) - (1-w) \log(1-w)), \quad (4-a)$$

$$Loss_s = \frac{1}{len(W)} \sum_{w \in T} w. \quad (4-b)$$

In Eq. (4-a), the loss term  $-w \log(w) - (1-w) \log(1-w)$  will push  $w$  close to 0 or 1 in the network training process [22]; and  $len()$  takes the length of  $W$ . The mean of all weights  $w \in M$  serves as the sparse loss as described in Eq. (4-b). A smaller  $Loss_s$  indicates more  $w$  values are closer to 0, namely the connectivity in super-PRNet will be sparser. We choose  $\alpha = 5e - 3$ ,  $\beta = 5e - 4$ , which are determined after tuning.

We collected and constructed a dataset consisting of 398 interferograms of NIH/3T3 cells with size of  $1024 \times 1024$  pixels with a home-built portable off-axis QPI system [29]. The corresponding ground truth phase maps are obtained by the conventional Fourier transform based method [6]. Before feeding into the network, the pixel value of interferograms is normalized to the range of 0 to 1. The ground truth phase maps are then normalized to the range of  $[0, 1]$  (i.e., unitless) by thresholding at 0 and 12 rad and dividing by 12 rad. Note that the maximum phase of 12 rad covers all the cell phase values present in the dataset. The number of interferogram-phase pairs contained in the training set, validation set, and test set are 276, 60, and 62, respectively. To reduce the computer memory during training, we cropped the image pairs into  $512 \times 512$  pixels. However, for validation and testing, the original size is kept. The Adam optimizer is used for training with a learning rate of 0.008. To balance between phase retrieval accuracy and network sparsity, the network is pretrained with only phase reconstruction  $Loss_t$  for the first 100 epochs and then trained with the synthesized loss  $Loss_*$  for the next 200 epochs. After training each epoch, the model's phase retrieval accuracy is validated using peak signal-to-noise ratio (PSNR) on the validation dataset. The training process took 4 hours on a GPU workstation (Intel Xeon Silver 4210R CPU  $[\times 2]$ , Nvidia RTX A6000 48GB  $[\times 2]$ ).

## C. NAS-PRNet from Pruning Super-PRNet

The connection weight set  $W$  in checkpoint with the highest validation PSNR is used for pruning super-PRNet to get NAS-PRNet. The pruning rules are as follows: (i) drop all the connections with weights  $w < \sigma$ , where  $\sigma$  is a threshold set at 0.5 after tuning; (ii) drop all decoder stages without any input features; and (iii) drop all decoder stages whose features are not used by any decoder stages. After pruning, the number of connections in super-PRNet (Fig. 3(a)) is significantly reduced to achieve NAS-PRNet with sparse connections (Fig. 3(b)). The number of connections reduced from 100 to 39, equivalent to reducing the connections by 61%. In NAS-PRNet, the lowest and the second lowest features ( $E_1$  and  $E_2$ ) in encoder take part in the formation of the second to last decoder feature ( $D_2$ ), and  $D_2$  along with other higher-level decoder features form the last decoder feature ( $D_1$ ). Therefore, a correction fusion of low-level and high-level features is important to ensure an accurate phase retrieval.

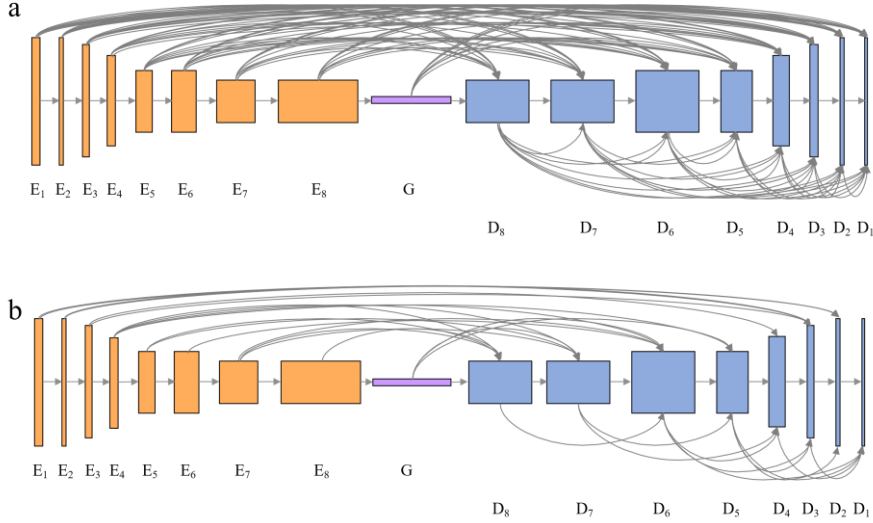


Fig. 3. (a) Connections in super-PRNet. (b) Connections in NAS-PRNet. Orange rectangles represent encoder stages, blue rectangles represent decoder stages.

In addition to applying the found connection scheme, NAS-PRNet differs from super-PRNet when producing the fused feature by removing  $w$  and  $bn()$  in Eq. (1), therefore, the fused feature  $T_l'$  of NAS-PRNet is:

$$T_l' = \sum_{m \in M_l^+} conv(f_{\downarrow}(m)) + \sum_{m \in M_l^-} f_{\uparrow}(conv(m)), \quad (5)$$

### 3. PHASE IMAGING RESULTS AND ANALYSIS

#### A. Phase Retrieval Accuracy and Computation Latency Analysis

NAS-PRNet was trained to obtain the final phase retrieval result. We trained NAS-PRNet following the same protocol as the super-PRNet but only used the phase reconstruction loss  $Loss_t$  for 200 epochs. Checkpoint with the best validation PSNR was saved and tested on the test set. When testing, the network output value in range 0-1 was multiplied by 12 rad to get the phase value, while PSNR was used to evaluate the phase retrieval accuracy. Computation latency of NAS-PRNet for output phase image of  $1024 \times 1024$  pixels was tested on a laptop (Intel i7-9750H CPU [ $\times 1$ ], Nvidia GeForce RTX 2060 6GB [ $\times 1$ ]). The testing result shows that NAS-PRNet has achieved PSNR of 36.1 dB and computation latency of 31 ms.

Network Model	PSNR	# of Parameters	Computation Latency
U-Net	34.7 dB	37.7M	373ms
SparseMask	32.5 dB	4.4M	28ms
NAS-PRNet	36.1 dB	5.0M	31ms

Table 1. Phase retrieval performance comparison between NAS-PRNet, U-Net, and SparseMask.

Using the same dataset, the performance of NAS-PRNet is compared with U-Net [30] and original SparseMask as shown in Table 1. U-Net features connections from each encoder stage to same-level decoder stage, and it has been frequently used for phase retrieval [13, 31]. We reproduced U-Net as used in Ref. [30], while the SparseMask for phase retrieval is generated by using the original search space, sparsity loss, and feature fusing style as used in Ref. [22] and incorporating other network structural changes proposed by us. Compared with U-Net, NAS-PRNet is 12 times faster in inference speed with 7.5 times fewer number of parameters. The PSNR of the phase maps inferred from NAS-PRNet is also higher than the U-Net (36.1 dB vs 34.7 dB). Compared with SparseMask, NAS-PRNet retrieved phase maps with a higher PSNR, thus indicating our modification to SparseMask is effective. In Fig. 4(a), we show one set of cell phase image comparison between ground truth and outputs from U-Net, SparseMask, and NAS-PRNet. Perceptually, the output from NAS-PRNet has a higher image fidelity when compared with the ground truth.

## B. Generalization Capability and Phase Unwrapping Analysis

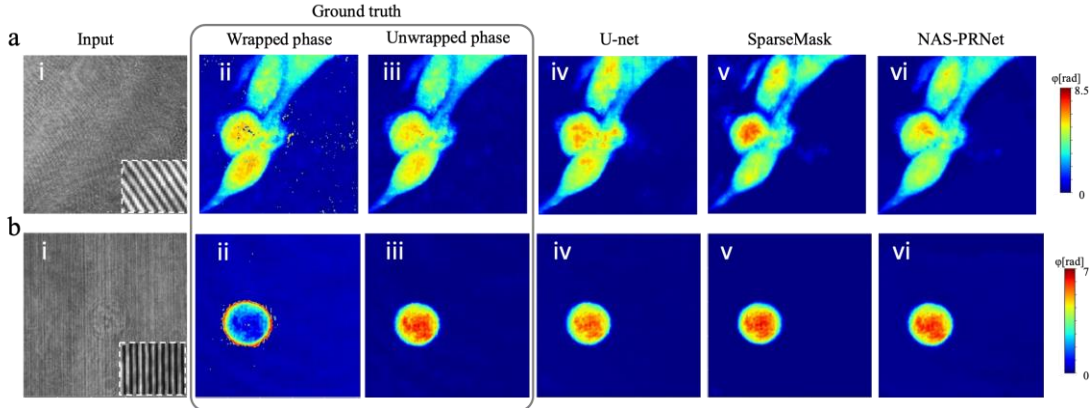


Fig. 4. Visual comparison of phase maps from ground truth, U-Net, SparseMask, and NAS-PRNet. (a) and (b) are representative phase maps from the NIH/3T3 dataset and the WBC dataset, respectively.

To explore the searched architecture’s capability in transferring into different off-axis QPI systems, we trained the NAS-PRNet on a white blood cell (WBC) dataset as reported in Ref. [32]. The WBC dataset has a different fringe pattern style (e.g., orientations, periods, and contrasts) compared with the NIH/3T3 dataset, as shown in the insets of Fig. 4(a.i) and (b.i). The WBC dataset includes 398 interferogram-phase pairs with size of  $960 \times 960$  pixels with 258 pairs used for training, 55 pairs used for validation, and 57 pairs used for testing. We re-trained NAS-PRNet, U-Net, SparseMask above. The training, validation, testing processes for these three models on the WBC dataset is the same as the NIH/3T3 dataset. The PSNRs for NAS-PRNet, U-Net, SparseMask are 42.9dB, 40.0dB, 42.4dB, separately. NAS-PRNet again outperforms U-Net and SparseMask. This indicates that the capability of fusing high-level and low-level features in NAS-PRNet can be potentially generalized to different off-axis QPI systems.

Note that when using the traditional Fourier-transform based phase retrieval method (i.e, the ground truth map), phase unwrapping (e.g., the widely used Goldstein algorithm) is required after obtaining the

wrapped phase map as shown in Fig. 4 (a.ii) and (b.ii). The phase unwrapping step using Goldstein algorithm takes around 528 ms for each phase map, as generated in Fig. 4 (a.iii) and (b.iii). However, our NAS-PRNet can directly output the unwrapped phase within around 31 ms, thus significantly saving the total image processing time. The phase unwrapping range of NAS-PRNet can be extended by using a training dataset with large phase values in the future. Moreover, NAS-PRNet can compensate aberration automatically without using a calibration phase map to simplify the phase imaging process.

#### 4. CONCLUSION

In conclusion, we have developed NAS-PRNet and optimized the architecture for phase retrieval with balanced output accuracy and inference speed. Compared with U-Net, NAS-PRNet has 7.5 times fewer parameter and 12 times higher inference speed, while the phase retrieval accuracy is similar. NAS-PRNet can be applied to a new style of fringe pattern measured by a different off-axis QPI system, thus indicating a good generalization capability. The current search space of NAS-PRNet is only limited to the connection scheme, but it can be further expanded to cover layer depth, layer manipulation, and so on, which may lead to the identification of an even better network architecture. In the future, we envision the light-weight NAS-PRNet enabled off-axis QPI systems will find many potential real-time imaging and metrology applications, such as profiling the morphology of living cells and quantifying their dynamics.

**Funding.** Hong Kong Innovation and Technology Fund (Grant Nos. ITS/148/20 and ITS/178/20FP), Croucher Foundation (CM/CT/CF/CIA/0688/19ay), and Research Grant Council of Hong Kong SAR (Grant No. 14209521).

**Disclosures.** The authors declare no conflicts of interest.

**Acknowledgements.** The authors are grateful to Mr. Wei Luo for providing us with the Lambo library for processing phase image datasets. The authors are also thankful to Mr. Guanyuan Zhao for his suggestions on using neural architecture search for phase retrieval.

**Author Contributions.** X.S., designed, implemented, and optimized the neural architecture search model and analyzed the results following guidance from R.Z. M.N., designed and built the quantitative phase microscope and performed imaging experiments. X.S and Y.Z. worked together on optimizing the efficiency of the neural network. X.S., and R.Z., wrote the manuscript with contribution from all the authors. R.Z., supervised the project.

**Data Availability.** The data and code are available from the corresponding author upon reasonable request.

#### Reference

1. G. Popescu, *Quantitative phase imaging of cells and tissues* (McGraw-Hill Education, 2011).
2. Y. Park, C. Depeursinge, and G. Popescu, "Quantitative phase imaging in biomedicine," *Nat Photonics* **12**, 578-589 (2018).
3. C. Zheng, D. Jin, Y. He, H. Lin, J. Hu, Z. Yaqoob, P. T. So, and R. Zhou, "High spatial and temporal resolution synthetic aperture phase microscopy," *Adv Photonics* **2**, 065002 (2020).
4. C. Edwards, R. Zhou, S.-W. Hwang, S. J. McKeown, K. Wang, B. Bhaduri, R. Ganti, P. J. Yunker, A. G. Yodh, J. A. Rogers, L. L. Goddard, and G. Popescu, "Diffraction phase microscopy: monitoring nanoscale dynamics in materials science [Invited]," *Appl Optics* **53**, G33-G43 (2014).
5. E. N. Leith, and J. Upatnieks, "Reconstructed Wavefronts and Communication Theory," *J Opt Soc Am* **52**, 1123-1130 (1962).
6. M. Takeda, H. Ina, and S. Kobayashi, "Fourier-Transform Method of Fringe-Pattern Analysis for Computer-Based Topography and Interferometry," *J Opt Soc Am* **72**, 156-160 (1982).
7. R. M. Goldstein, H. A. Zebker, and C. L. Werner, "Satellite Radar Interferometry - Two-Dimensional Phase Unwrapping," *Radio Sci* **23**, 713-720 (1988).

8. P. Ferraro, S. De Nicola, A. Finizio, G. Coppola, S. Grilli, C. Magro, and G. Pierattini, "Compensation of the inherent wave front curvature in digital holographic coherent microscopy for quantitative phase-contrast imaging," *Appl Optics* **42**, 1938-1946 (2003).
9. H.-Y. Chen, S.-H. Hsu, W.-J. Hwang, and C.-J. Cheng, "An efficient FPGA-based parallel phase unwrapping hardware architecture," *IEEE Trans Comput Imaging* **3**, 996-1007 (2017).
10. H. Pham, H. Ding, N. Sobh, M. Do, S. Patel, and G. Popescu, "Off-axis quantitative phase imaging processing using CUDA: toward real-time applications," *Biomed. Opt. Express* **2**, 1781-1793 (2011).
11. Y. Yao, X. Shu, and R. Zhou, "Deep learning based phase retrieval in quantitative phase microscopy," *Proc. SPIE* **11351**, 113510W (2020).
12. T. Chang, D. Ryu, Y. Jo, G. Choi, H. S. Min, and Y. Park, "Calibration-free quantitative phase imaging using data-driven aberration modeling," *Opt Express* **28**, 34835-34847 (2020).
13. K. Wang, J. Dou, Q. Kemaoy, J. Di, and J. Zhao, "Y-Net: a one-to-two deep learning framework for digital holographic reconstruction," *Opt Lett* **44**, 4765-4768 (2019).
14. T. Elsken, J. H. Metzen, and F. Hutter, "Neural architecture search: a survey," *J Mach Learn Res* **20**, 1997-2017 (2019).
15. M. S. Tanveer, M. U. K. Khan, and C.-M. Kyung, "Fine-tuning darts for image classification," in *International Conference on Pattern Recognition (ICPR)* (2021), pp. 4789-4796.
16. A. Howard, M. Sandler, G. Chu, L.-C. Chen, B. Chen, M. Tan, W. Wang, Y. Zhu, R. Pang, V. Vasudevan, Quoc, and H. Adam, "Searching for MobileNetV3," in *IEEE International Conference on Computer Vision (ICCV)* (2019), pp. 1314-1324.
17. B. Zoph, V. Vasudevan, J. Shlens, and Q. V. Le, "Learning Transferable Architectures for Scalable Image Recognition," in *IEEE / CVF Computer Vision and Pattern Recognition Conference (CVPR)* (2018), pp. 8697-8710.
18. C. X. Liu, L. C. Chen, F. Schroff, H. Adam, W. Hua, A. Yuille, and F. F. Li, "Auto-DeepLab: Hierarchical Neural Architecture Search for Semantic Image Segmentation," in *IEEE / CVF Computer Vision and Pattern Recognition Conference (CVPR)* (2019), pp. 82-92.
19. W. Chen, X. Gong, X. Liu, Q. Zhang, Y. Li, and Z. Wang, "FasterSeg: Searching for Faster Real-time Semantic Segmentation," in *International Conference on Learning Representations (ICLR)* (2020).
20. X. Yan, W. Jiang, Y. Shi, and C. Zhuo, "Ms-nas: Multi-scale neural architecture search for medical image segmentation," in *International Conference on Medical Image Computing and Computer Assisted Intervention (MICCAI)* (2020), pp. 388-397.
21. V. Nekrasov, H. Chen, C. H. Shen, and I. Reid, "Fast Neural Architecture Search of Compact Semantic Segmentation Models via Auxiliary Cells," in *IEEE / CVF Computer Vision and Pattern Recognition Conference (CVPR)* (2019), pp. 9118-9127.
22. H. K. Wu, J. G. Zhang, and K. Q. Huang, "SparseMask: Differentiable Connectivity Learning for Dense Image Prediction," in *IEEE International Conference on Computer Vision (ICCV)* (2019), pp. 6767-6776.
23. H. Liu, K. Simonyan, and Y. Yang, "Darts: Differentiable architecture search," in *International Conference on Learning Representations (ICLR)* (2018).
24. H. Zhao, J. Shi, X. Qi, X. Wang, and J. Jia, "Pyramid scene parsing network," in *IEEE / CVF Computer Vision and Pattern Recognition Conference (CVPR)* (2017), pp. 2881-2890.
25. M. Everingham, S. Eslami, L. Van Gool, C. K. Williams, J. Winn, and A. Zisserman, "The pascal visual object classes challenge: A retrospective," *Int J Comput Vision* **111**, 98-136 (2015).
26. M. Sandler, A. Howard, M. L. Zhu, A. Zhmoginov, and L. C. Chen, "MobileNetV2: Inverted Residuals and Linear Bottlenecks," in *IEEE / CVF Computer Vision and Pattern Recognition Conference (CVPR)* (2018), pp. 4510-4520.
27. A. Krizhevsky, "Convolutional deep belief networks on cifar-10," in [www.cs.toronto.edu/~kriz/conv-cifar10-aug2010.pdf](http://www.cs.toronto.edu/~kriz/conv-cifar10-aug2010.pdf).
28. S. Van der Jeught, P. G. G. Muysshondt, and I. Lobato, "Optimized loss function in deep learning profilometry for improved prediction performance," *JPhys Photonics* **3** (2021).

29. X. Shu, Y. Zhang, M. Niu, W. Luo, and R. Zhou, "Compact and ease-of-use quantitative phase microscopy for real-time live-cell imaging," Proc. SPIE **11970**, 1197004 (2022).
30. O. Ronneberger, P. Fischer, and T. Brox, "U-Net: Convolutional Networks for Biomedical Image Segmentation," in *International Conference on Medical Image Computing and Computer Assisted Intervention (MICCAI)* (2015), pp. 234-241.
31. I. Choi, K. Lee, and Y. Park, "Compensation of aberration in quantitative phase imaging using lateral shifting and spiral phase integration," Opt Express **25**, 30771-30779 (2017).
32. X. Shu, S. Sansare, D. Jin, X. Zeng, K.-Y. Tong, R. Pandey, and R. Zhou, "Artificial-Intelligence-Enabled Reagent-Free Imaging Hematology Analyzer," Adv Intell Syst **3**, 2000277 (2021).